

High-Efficiency Polycrystalline Perovskite Light-Emitting Diodes Based on Mixed Cations

Himchan Cho,^{†,§,#} Joo Sung Kim,^{†,#} Christoph Wolf,^{||} Young-Hoon Kim,^{†,‡,§} Hyung Joong Yun,[⊥] Su-Hun Jeong,^{†,‡} Aditya Sadhanala,[¶] Vijay Venugopalan,[¶] Jin Woo Choi,[□] Chang-Lyoul Lee,[□] Richard H. Friend,[¶] and Tae-Woo Lee^{*,†,‡,§,||}

[†]Department of Materials Science and Engineering, [‡]Research Institute of Advanced Materials, and [§]BK21 PLUS SNU Materials Division for Educating Creative Global Leaders, Seoul National University, 1 Gwanak-ro, Gwanak-gu, Seoul 08826, Republic of Korea

^{||}Center for Quantum Nanoscience, Institute for Basic Science (IBS), 52 Ewhayeodae-gil, Seodaemun-gu, Seoul 03760, Republic of Korea

[⊥]Advance Nano Research Group, Korea Basic Science Institute (KBSI), 169-148 Gwahak-ro, Yuseong-gu, Daejeon 34133, Republic of Korea

[¶]Cavendish Laboratory, University of Cambridge, JJ Thomson Avenue, Cambridge CB3 0HE, United Kingdom

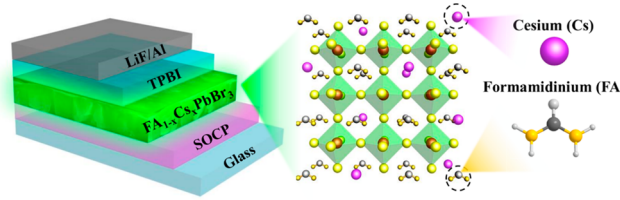
[□]Advanced Photonics Research Institute (APRI), Gwangju Institute of Science and Technology (GIST), 261 Cheomdan-gwagiro, Buk-gu, Gwangju 61005, Republic of Korea

Supporting Information

ABSTRACT: We have achieved high-efficiency polycrystalline perovskite light-emitting diodes (PeLEDs) based on formamidinium (FA) and cesium (Cs) mixed cations without quantum dot synthesis. Uniform single-phase $\text{FA}_{1-x}\text{Cs}_x\text{PbBr}_3$ polycrystalline films were fabricated by one-step formation with various FA:Cs molar proportions; then the influences of chemical composition on film morphology, crystal structure, photoluminescence (PL), and electroluminescence (EL) were systematically investigated. Incorporation of Cs^+ cations in FAPbBr_3 significantly reduced the average grain size (to 199 nm for FA:Cs = 90:10) and trap density; these changes consequently increased PL quantum efficiency (PLQE) and PL lifetime of $\text{FA}_{1-x}\text{Cs}_x\text{PbBr}_3$ films and current efficiency (CE) of PeLEDs. Further increase in Cs molar proportion from 10 mol % decreased crystallinity and purity, increased trap density, and correspondingly decreased PLQE, PL lifetime, and CE. Incorporation of Cs also increased photostability of $\text{FA}_{1-x}\text{Cs}_x\text{PbBr}_3$ films, possibly due to suppressed formation of light-induced metastable states. $\text{FA}_{1-x}\text{Cs}_x\text{PbBr}_3$ PeLEDs show the maximum CE = 14.5 cd A^{-1} at FA:Cs = 90:10 with very narrow EL spectral width (21–24 nm); this is the highest CE among FA-Cs-based PeLEDs reported to date. This work provides an understanding of the influences of Cs incorporation on the chemical, structural, and luminescent properties of FAPbBr_3 polycrystalline films and a breakthrough to increase the efficiency of $\text{FA}_{1-x}\text{Cs}_x\text{PbBr}_3$ PeLEDs.

KEYWORDS: cation hybridization, formamidinium lead bromide, A-site cations, alternative emitters, composition control

High-efficiency perovskite LEDs based on FA-Cs mixed cations



Metal halide perovskites (MHPs) are semiconducting materials that have provided significant breakthroughs in diverse electronics applications including light-emitting diodes (LEDs),^{1–4} solar cells,⁵ lasers,⁶ and synaptic devices.⁷ Use of MHPs in solar cell research has achieved a certified power conversion efficiency (PCE) of >20%,⁸ which has been attributed to the advantages of MHPs as excellent light harvesters, such as broad light absorption spectra with sharp band edge, small exciton binding energy, and long (micrometer-scale) charge-carrier diffusion lengths.^{9,10} MHPs are also promising as light-emitting materials with high

color purity for next-generation natural-color displays, due to narrow spectral width (full width at half-maximum (fwhm) < 20 nm), tunable emission wavelength ($400 \leq \lambda \leq 780 \text{ nm}$), comparable ionization energy (IE), with those of common semiconducting materials in organic LEDs (OLEDs), and low material cost.^{1–4,11–20}

Received: January 16, 2018

Accepted: March 1, 2018

Published: March 1, 2018

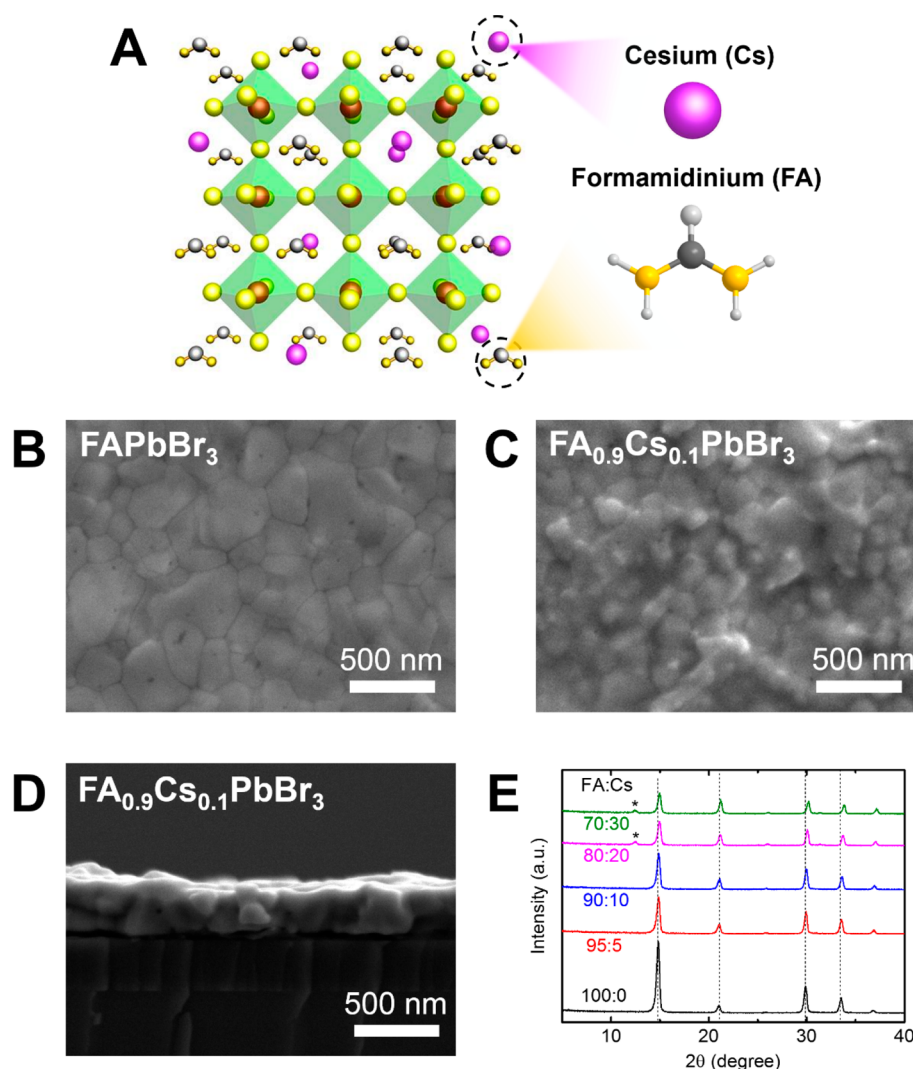


Figure 1. (A) Crystal structure of MHPs based on FA⁺ and Cs⁺ cations. SEM images of (B) pure FAPbBr₃ and (C) FA_{0.9}Cs_{0.1}PbBr₃ polycrystalline films. (D) SEM image of a cross-section of an FA_{0.9}Cs_{0.1}PbBr₃ polycrystalline film on an SOCP layer. (E) XRD patterns of FA_{1-x}Cs_xPbBr₃ polycrystalline films with various FA:Cs molar ratios (curves are offset for clarity).

After pioneering reports on MAPbBr₃ MHP LEDs (PeLEDs) that exhibited high brightness (>100 cd m⁻²) at room temperature (maximum current efficiency (CE_{max}) = 0.3 and 0.577 cd A⁻¹),^{3,4} the electroluminescence (EL) efficiency of PeLEDs has been rapidly increased to CE_{max} = 42.9 cd A⁻¹ (maximum external quantum efficiency (EQE_{max}) = 8.53%) within only 1.5 years, by fine stoichiometry control to remove luminescence quenchers and by nanograin engineering to reduce MHP grain size.² Also, diverse approaches such as flexible anodes,^{11,17} quasi-2D structure,^{12–15,19–21} and colloidal quantum dots (QDs)^{16,18,22–25} have shown the great potential of PeLEDs for highly efficient flexible displays. Particularly, incorporation of larger organic ammonium cations than MA⁺ cations enabled realization of highly efficient and stable infrared PeLEDs (EQE_{max} = 8.8%,¹³ 11.7%¹⁴) and green PeLEDs (CE_{max} = 17.1 cd A⁻¹).¹⁵

MHPs generally have the chemical formula AMX₃, where A is a monovalent cation [e.g., methylammonium (MA) CH₃NH₃⁺, cesium Cs⁺, formamidinium (FA) CH(NH₂)₂⁺], M is a divalent transition metal [e.g., Pb²⁺, Sn²⁺], and X is a halide anion [Cl⁻, Br⁻, I⁻].¹ Because of the strong dependence of optoelectronic and structural properties of MHPs on the

ionic components, the control of A-site cations^{12–15,26,27} and halide anions^{4,28,29} has been widely studied to control band gap and increase device efficiency and stability.

Although MAPbBr₃-based PeLEDs have shown EL efficiency that is even comparable to that of organic LEDs,² MA-based MHPs suffer from susceptibility to degradation by heat or moisture.^{30,31}

To avoid these problems and stabilize MHP crystal structure, stable A-site cations such as FA⁺ and Cs⁺ have been evaluated as replacements for MA⁺. The use of thermally stable MHPs enables the application of high-temperature fabrication processes and reduces thermal degradation of MHP layers in PeLEDs during fabrication processes and device operation.³² FAPbX₃ has a larger lattice constant than does MAPbX₃ due to the larger ionic radius of FA⁺ (2.79 Å) than that of MA⁺ (2.70 Å); this difference increases the structural and thermal stability of the MHP (thermal decomposition temperature ≈ 150 °C for MAPbBr₃ and ≈ 200 °C for FAPbBr₃).^{33–35}

FAPbI₃ was suggested as an alternative to MAPbI₃ for light harvesting because FAPbI₃ has superior thermal stability, reduced band gap, and longer carrier lifetime, but it may spontaneously form a nonperovskite δ-phase at room temper-

ature.^{34–36} In contrast to FAPbI₃, FAPbBr₃ has a relatively stable pseudocubic structure,³³ higher charge-carrier mobility (62 cm² V^{−1} s^{−1} for FAPbBr₃ single crystals), and lower trap density (9.6 × 10⁹ cm^{−3}³⁴ than does MAPbBr₃ (24 cm² V^{−1} s^{−1} and 3 × 10¹⁰ cm^{−3} for single crystals).³⁷ Based on these advantages, FAPbBr₃-based PeLEDs were constructed by two-step deposition (CE_{max} = 2.65 cd A^{−1}³⁸) and by FAPbBr₃ QD synthesis (CE_{max} = 6.4,²³ 9.16,¹⁶ and 13.02 cd A^{−1}²⁵). The CE_{max} of FAPbBr₃ QD PeLED (13.02 cd A^{−1}²⁵) is comparable to that of MAPbBr₃ QD PeLED (15.5 cd A^{−1}¹⁸); however, the CE_{max} of polycrystalline FAPbBr₃ PeLED (2.65 cd A^{−1}³⁸) is much poorer than that of polycrystalline MAPbBr₃ PeLED (CE_{max} = 42.9 cd A^{−1}²). Therefore, further studies to optimize the FAPbBr₃ polycrystalline layer and device architecture are needed.

Cs-based all-inorganic MHPs have also been studied to reduce the chemical instability of MA-based MHPs.^{39–42} CsPbX₃ MHPs have a much higher thermal decomposition temperature (~580 °C for CsPbBr₃) than does MAPbX₃ (~220 °C for MAPbBr₃).^{40,43} In addition, CsPbBr₃ has excellent optoelectronic properties such as a narrow emission spectrum (17 ≤ fwhm ≤ 19 nm),^{39,41} high PL quantum efficiency (PLQE) up to 90% (in solution),^{39,41} high electron mobility (~1000 cm² V^{−1} s^{−1}), and long carrier relaxation lifetime (~2.5 μs in single crystals).⁴⁴ To take full use of these advantages, diverse approaches to achieve stable and efficient CsPbBr₃ PeLEDs have been reported.^{42,45,46} However, pure CsPbBr₃ polycrystalline layers cannot be readily formed into thick uniform films, so polycrystalline pure CsPbBr₃ PeLEDs without additives have shown low EL efficiency (CE_{max} = 0.035, 0.57, and 5.39 cd A^{−1}).^{42,45,46}

To overcome the disadvantages of MHPs based on pure FA or Cs, and thereby improve device stability and efficiency, the development of mixed-cation-based MHP systems has been considered.^{22,35,36,47,48} Hybridization of FA⁺ and Cs⁺ cations and control of their stoichiometry can modify the structural and chemical characteristics of MHPs and thus increase device efficiency and stability.^{22,35,36,47,48} Partially alloying Cs⁺ cations into unstable FAPbI₃ or FAPbI_{3–x}Br_x significantly reduced its susceptibility to degradation by heat, light, and moisture; increased its phase stability due to entropic stabilization and modified its tolerance factor (0.94–0.98) by lattice contraction; and increased its PCE by reducing trap density.^{35,47,48} Furthermore, FA_{1–y}Cs_yPb(Br_{1–x}I_x)₃ systems have the highest crystallinity and charge-carrier mobility and the longest charge-carrier lifetime in the optimal range of stoichiometry (0.10 < y < 0.30).³⁶ Recently, FA-Cs mixed-cation PeLEDs based on MHP QDs have shown a CE_{max} of 10.09 cd A^{−1}.²² However, insulating ligands around QDs hinder charge injection into QDs, and low concentration of dispersed MHP QD solutions impairs the formation of thick uniform films. Also, nonradiative recombination by surface defects on QDs and a complex process to synthesize QDs are strong impediments to their application in PeLEDs. Therefore, highly bright and efficient mixed-cation PeLEDs should be developed based on a simple process to fabricate polycrystalline MHP layers instead of using QD synthesis.

Here, we demonstrate fabrication of high-efficiency polycrystalline PeLEDs based on FA-Cs mixed cations (Figure 1A) by one-step formation of uniform FA_{1–x}Cs_xPbBr₃ polycrystalline films. Partial substitution of Cs⁺ cations (≤10 mol %) for FA⁺ cations significantly decreased MHP grain size and trap density and thereby improved PLQE of MHP films and EL

efficiency of PeLEDs; the FA_{1–x}Cs_xPbBr₃ PeLEDs at the optimized molar ratio of FA:Cs = 90:10 exhibited a much higher CE_{max} of 14.5 cd A^{−1} than those of pure FAPbBr₃ PeLEDs (CE_{max} = 7.96 cd A^{−1}). At a Cs molar proportion of >10%, CE gradually decreased, due to the decrease in PLQE, which was ascribed to decreased crystallinity and increased trap density, as suggested by X-ray diffraction (XRD), PL lifetime, and temperature-dependent PL results. Gradual changes in XRD patterns, X-ray photoelectron spectroscopy (XPS), steady-state PL, and EL spectra indicate that the FA_{1–x}Cs_xPbBr₃ forms a single phase without phase separation. This study offers simple methods to increase luminescence efficiency of polycrystalline films and PeLEDs based on FA and Cs.

RESULTS AND DISCUSSION

The partial substitution of Cs⁺ cations for FA⁺ cations significantly changed the film morphology (Figure 1B,C). The pure FAPbBr₃ polycrystalline films had grain sizes ranging from 100 to 600 nm (average = 325 nm) (Figure S1A). Use of 10–40 mol % Cs⁺ cations significantly reduced MHP grain size (Figure S1B, Figure S2); the FA_{0.9}Cs_{0.1}PbBr₃ polycrystalline films showed much more closely packed grains with smaller grain size (average = 199 nm) (Figure S1B) than did pure FAPbBr₃ films. The FA_{1–x}Cs_xPbBr₃ polycrystalline films were 200–300 nm thick (Figure 1D).

The crystal structures of the fabricated FA_{1–x}Cs_xPbBr₃ polycrystalline films and their changes with FA:Cs molar ratio were investigated by measuring XRD patterns (Figure 1E, Figures S3, S4, and Table S1). The XRD patterns of FAPbBr₃ films exhibited (100), (110), (200), and (210) peaks at 14.84°, 21.04°, 29.88°, and 33.54°, which are consistent with a pseudocubic *Pm* $\bar{3}$ *m* phase and agree with a previous report.³³ The lattice constant of FAPbBr₃ was calculated to be 5.962 Å, which is slightly larger than the lattice constant of MAPbBr₃ (5.88–5.92 Å).^{2,33} As the Cs molar proportion in the FA_{1–x}Cs_xPbBr₃ films increased, the peaks shifted to higher 2θ positions (Figure 1E, Figure S3); this trend indicates that the lattice constant gradually decreased from 5.962 Å (for FAPbBr₃) to 5.907 Å (for FA_{0.7}Cs_{0.3}PbBr₃) because of the much lower ionic radius of Cs⁺ cations (1.81 Å) than of FA⁺ cations (2.79 Å) (Figure S4A, Table S1);⁴⁹ that is, this FA_{1–x}Cs_xPbBr₃ system approximately follows Vegard's law that states that the lattice constant of a solid solution of two constituents depends linearly on its molar fraction.⁵⁰ The gradual shift in XRD peak position also implies the formation of single-phase FA_{1–x}Cs_xPbBr₃ crystals without phase segregation. Also, the intensities of the (100), (200), and (210) peaks gradually decreased as the Cs molar proportion increased, although the (110) peaks did not (Figure S3A–C); these changes indicate that the increase in Cs molar proportion decreases the crystallinity of FA_{1–x}Cs_xPbBr₃ films and alters the preferred orientation of crystallites. The gradual decrease in crystallinity is also consistent with Vegard's law because CsPbBr₃ films showed much lower XRD peak intensities⁴⁶ than did FA_{1–x}Cs_xPbBr₃ films. The crystallite sizes (Table S1) of FA_{1–x}Cs_xPbBr₃ films were calculated from the fwhm of XRD peaks by using the Scherrer equation.² The average fwhm slightly decreased as the Cs molar proportion increased (Figure S4B, Table S1); this trend concurs well with a previous report.³⁶ An inconsistency between the calculated crystallite size from XRD data (Table S1) and the apparent grain size in scanning electron microscope (SEM) images (Figure S1) may

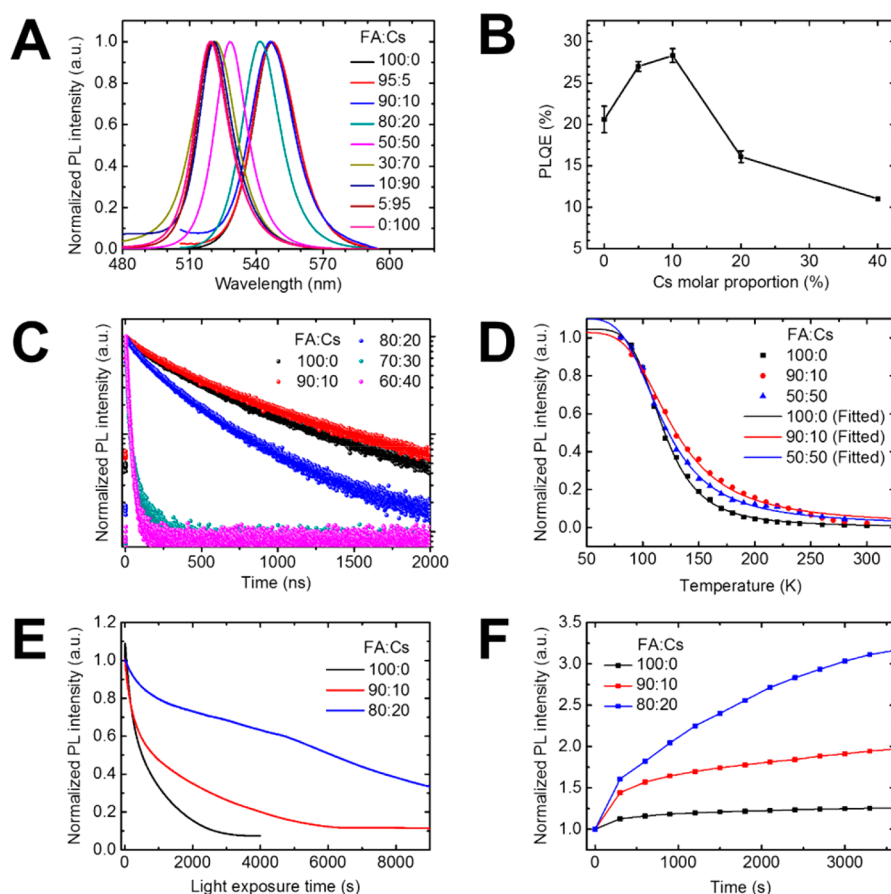


Figure 2. (A) Normalized PL spectra, (B) PLQE, (C) PL lifetime curves, and (D) temperature-dependent PL intensity of $\text{FA}_{1-x}\text{Cs}_x\text{PbBr}_3$ polycrystalline films with varying FA:Cs molar ratio. (E) Photostability of $\text{FA}_{1-x}\text{Cs}_x\text{PbBr}_3$ polycrystalline films under continuous light exposure. A continuous-output xenon arc lamp with a power of 150 W (405 nm wavelength) was used as an excitation source. (F) Recovery of PL intensity in the dark after photostability measurement. The PL intensity was measured at intervals of 300 s.

occur because the grains consist of many crystallites or because the instrument contribution to peak broadening is not negligible. Furthermore, films with FA:Cs = 80:20 and 70:30 showed a small XRD peak at $\sim 12.5^\circ$ (Figure 1E, Figure S3D; marked with an asterisk); we assigned this peak to PbBr_2 after considering previous reports.^{47,51} The emergence of a PbBr_2 peak implies that the reaction between FABr/CsBr and PbBr_2 was incomplete at a Cs molar proportion of $\geq 20\%$.

Before fabricating $\text{FA}_{1-x}\text{Cs}_x\text{PbBr}_3$ PeLEDs, we studied optical properties of the $\text{FA}_{1-x}\text{Cs}_x\text{PbBr}_3$ polycrystalline films. As the Cs molar proportion increased from FA:Cs = 100:0 to 0:100, the PL peaks blue-shifted from 537 nm to 519 nm (Figure 2A, Figures S5A). The optical band gap of the $\text{FA}_{1-x}\text{Cs}_x\text{PbBr}_3$ films was calculated using a Tauc plot of their absorption spectra (Figure S5B,C). As the Cs molar proportion increased from 0% to 40%, the optical band gap linearly increased from ~ 2.29 eV to ~ 2.32 eV. These changes correspond to a gradual shift in XRD peak positions (Figure 1E, Figure S3) and confirm the presence of single-phase $\text{FA}_{1-x}\text{Cs}_x\text{PbBr}_3$ crystals. The gradual changes in the PL peak wavelength and the optical band gap (Figure S5) are attributed to gradual change in the crystal structure; the incorporation of Cs in FAPbBr_3 causes reduction of the Br–Pb–Br angle (octahedral tilting) and consequently reduces the extent of Pb–Br orbital overlap.⁵² The reduction in the Pb–Br orbital overlap pushes the valence band maximum (VBM) and conduction

band minimum toward lower energies and thereby increases the optical band gap.⁵²

To study how Cs incorporation affects PL intensity, absolute PLQEs of $\text{FA}_{1-x}\text{Cs}_x\text{PbBr}_3$ films were measured. To prevent PLQE loss caused by glass substrates and self-organized conducting polymer (SOC) bottom layers, $\text{FA}_{1-x}\text{Cs}_x\text{PbBr}_3$ films were deposited directly on quartz substrates. As the Cs molar proportion increased, the average PLQE (over 10–12 measurements) increased from 20.6% at FA:Cs = 100:0, to 28.3% at FA:Cs = 90:10, then decreased to 16.1% at FA:Cs = 80:20 and to 11% at FA:Cs = 60:40 (laser power density = 900 mW cm^{-2}) (Figure 2B, Table S2).

The trend in PL lifetime of $\text{FA}_{1-x}\text{Cs}_x\text{PbBr}_3$ films (quartz/ $\text{FA}_{1-x}\text{Cs}_x\text{PbBr}_3$ /poly(methyl methacrylate) (PMMA)) was the same as the trend in PLQE (Figure 2C). The PL lifetime curves were obtained using time-correlated single-photon counting (TCSPC) and analyzed using biexponential fitting.⁵³ Fitting results include PL lifetimes τ and fractions f for fast-decay (τ_1 , f_1) and slow-decay (τ_2 , f_2) components and intensity-weighted average lifetime τ_{av} (Table S3). τ_{av} increased from 573.0 ns to 623.1 ns as the Cs molar proportion increased from 0% to 10%. As the Cs molar proportion further increased from 10%, τ_{av} gradually decreased to 17.5 ns (at FA:Cs = 60:40) and f_1 gradually increased from 10.9% to 71.2%. The PL lifetime curves were also plotted separately to exclude different background noise levels (Figure S6). The exciton diffusion length of the $\text{FA}_{0.9}\text{Cs}_{0.1}\text{PbBr}_3$ polycrystalline film (on quartz)

was calculated as 114 nm by using a decay rate from the PL lifetime curve of quartz/FA_{0.9}Cs_{0.1}PbBr₃/PMMA and a 1D diffusion model as reported previously.²

To gain insight into nonradiative pathways in FA_{1-x}Cs_xPbBr₃ polycrystalline films, we investigated the dependence of PL intensity, I_{PL} [a.u.] (normalized), on temperature T [K] (Figure 2D). As T increases, I_{PL} of MHP films decreases via two luminescence quenching pathways: thermal dissociation of excitons and trap-assisted nonradiative recombination.⁴⁶ The amounts of thermal quenching of I_{PL} were comparable for all films at low T (80–100 K), where the quenching pathways were just slightly activated. As T increased, the quenching pathways became more active, and thereby the difference in the amount of thermal quenching became larger. Overall, I_{PL} was higher in FA_{0.9}Cs_{0.1}PbBr₃ films than in pure FAPbBr₃ films and FA_{0.5}Cs_{0.5}PbBr₃ films. To analyze the PL quenching of FA_{1-x}Cs_xPbBr₃ polycrystalline films systematically, the temperature-dependent I_{PL} curves were fitted to a modified Arrhenius equation:⁵⁴

$$\frac{I_{\text{PL}}}{I_{\text{PL},0}} = \frac{1}{1 + A \exp(-E_{\text{a,PL}}/(k_{\text{B}}T))} \quad (1)$$

where $I_{\text{PL},0}$ is the PL intensity at 0 K, $k_{\text{B}} = 8.617 \times 10^{-2}$ meV K⁻¹ is the Boltzmann constant, T is absolute temperature, $E_{\text{a,PL}}$ [meV] is the activation energy of PL quenching processes, and A [a.u.] is a parameter that expresses the effect of thermally activated quenching processes on PL intensity. Fitting results showed that the FA_{0.9}Cs_{0.1}PbBr₃ films had smaller $A = 148.67$ than FAPbBr₃ (1417.48) and FA_{0.5}Cs_{0.5}PbBr₃ (211.72), whereas the samples had comparable $E_{\text{a,PL}}$ ($54.8 \leq E_{\text{a,PL}} \leq 73.9$ meV) (Table S4). These results can be interpreted to mean that (i) the exciton binding energies of the three FA_{1-x}Cs_xPbBr₃ films are comparable and that (ii) the FA_{0.9}Cs_{0.1}PbBr₃ film was the least affected by the thermally induced quenching processes such as trap-assisted nonradiative recombination.

Based on the results of PLQE, PL lifetime, and temperature-dependent PL measurement (Figure 2B,C,D), we posit that the increase in PLQE and PL lifetime and the suppression of thermally induced PL quenching by incorporating a small proportion (≤ 10 mol %) of Cs may be attributed to consequent reduction in MHP grain size (average: ~ 325 nm in FAPbBr₃ and ~ 199 nm in FA_{0.9}Cs_{0.1}PbBr₃) and trap density. The reduction of grain size strengthens spatial confinement of excitons or charge carriers in the grains (Figure S1) and thus increases PLQE.^{2,55} Also, the FA_{0.9}Cs_{0.1}PbBr₃ film may have a smaller density of trap states than does the FAPbBr₃ film,³⁵ although the FA_{0.9}Cs_{0.1}PbBr₃ film has lower crystallinity than does the FAPbBr₃ film. When trap density decreases, PLQE and τ_{av} of MHP films can increase and thermally induced PL quenching can be suppressed. Further theoretical studies are required to clearly understand the physical origin of the reduction in trap density. In contrast, the decrease in PLQE and τ_{av} at a Cs molar proportion of $>10\%$ may be a result of decreased crystallinity and purity (*i.e.*, higher PbBr₂ concentration) and of consequently increased trap density and trap-assisted nonradiative recombination. The gradual decrease in crystallinity with increasing Cs molar proportion and the incomplete reaction at a Cs molar proportion of $>20\%$ (Figure 1E, Figure S3) support this proposition; the density of defect sites in MHP films increases as crystallinity decreases,⁵⁶ and the defects often create deep trap states.^{57,58}

The incorporation of Cs also increased photostability of FA_{1-x}Cs_xPbBr₃ films. PL intensity of the films was measured continuously during exposure to light in ambient conditions (Figure 2E). The PL intensity of the FAPbBr₃ film abruptly decreased to 6.1% of the initial intensity at 2000 s. The photostability of FA_{1-x}Cs_xPbBr₃ films gradually increased as Cs molar proportion increased; the FA_{0.9}Cs_{0.1}PbBr₃ and FA_{0.8}Cs_{0.2}PbBr₃ films retained 24.0% and 80.3% of their initial PL intensities at 2000 s, respectively. Possible origins of the PL decrease are decomposition of FA_{1-x}Cs_xPbBr₃ crystals, structural modulation of Pb–Br octahedral frameworks,⁵⁹ formation of metastable trap states (localized polaronic states),⁶⁰ and localized stoichiometric variations in bromide content.^{61,62} To determine whether the PL decrease is a result of decomposition of FA_{1-x}Cs_xPbBr₃, the steady-state PL and absorption spectra (Figure S7) and XRD patterns (Figure S8) of FA_{1-x}Cs_xPbBr₃ films were measured before and after the photostability measurement. The PL peak positions and the absorption spectra did not change, the XRD patterns were almost unchanged, and no PbBr₂ peak emerged after the photostability measurement. Therefore, the decomposition of FA_{1-x}Cs_xPbBr₃ was eliminated as a possible origin of the PL decrease. The effect of environment on the photostability was examined by comparing the photostability of FA_{1-x}Cs_xPbBr₃ films with and without glass encapsulation performed in a nitrogen atmosphere (Figure S9). The trend in photostability with increasing Cs molar proportion was consistent in both environments (air and nitrogen). Unexpectedly, the nitrogen atmosphere did not improve the photostability of FA_{1-x}Cs_xPbBr₃ films; we attribute this to the following: (1) the PL decrease by light exposure did not accompany the decomposition of FA_{1-x}Cs_xPbBr₃ that can be accelerated by oxygen and moisture;⁶³ (2) the oxygen boost effect⁶⁴ that increases the PLQE of FA_{1-x}Cs_xPbBr₃ films can compensate the PL decrease by light exposure in air.

Right after the photostability measurement, the PL intensity of FA_{1-x}Cs_xPbBr₃ films was measured at intervals of 300 s while being stored in the dark in ambient conditions (Figure 2F). The light source was turned on only for several seconds at each measurement. In all FA_{1-x}Cs_xPbBr₃ films the PL intensity increased very gradually; this response indicates that the PL decrease by continuous light exposure was not attributed to decomposition of FA_{1-x}Cs_xPbBr₃, but to formation of (or transformation into) light-induced metastable states (or structures)^{59–62} that can return to their original states very slowly (on the order of minutes or hours). We speculate that the incorporation of Cs may inhibit the formation of light-induced states and consequently increase photostability. The increased photostability might also be related to lattice contraction or octahedral tilting; these structural changes can influence the bond strengths and the orbital overlap between the cations (FA⁺, Cs⁺, Pb²⁺) and Br⁻ anions.^{22,35,52} Despite the higher trap density of the FA_{0.8}Cs_{0.2}PbBr₃ film than that of the FA_{0.9}Cs_{0.1}PbBr₃ film, the FA_{0.8}Cs_{0.2}PbBr₃ film showed a better photostability; it implies that formation of light-induced metastable states are not affected by the trap density. To reveal the precise origin of increased photostability by Cs incorporation, further studies are required.

We constructed an energy level diagram (Figure 3) based on ultraviolet photoelectron spectroscopy (UPS) spectra (Figure S10) of FA_{1-x}Cs_xPbBr₃ polycrystalline films. To exclude the effect of 1,3,5-tris(*N*-phenylbenzimidazol-2-yl)benzene (TPBI) molecules at the film surfaces, the FA_{1-x}Cs_xPbBr₃ polycrystal-

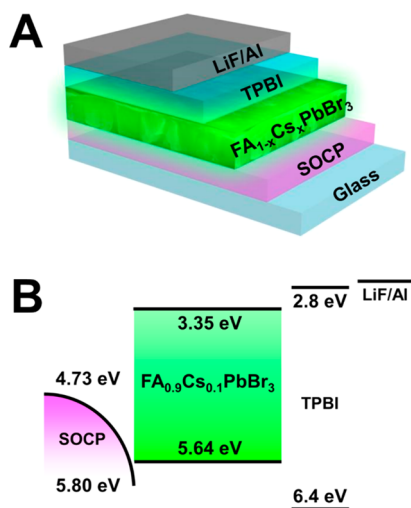


Figure 3. (A) Schematic diagram of device structure of $\text{FA}_{1-x}\text{Cs}_x\text{PbBr}_3$ polycrystalline PeLEDs. (B) Schematic energy level diagram.

line films were fabricated using a solvent-based nanocrystal pinning process that uses pure chloroform to wash out dimethyl sulfoxide (DMSO). We analyzed the changes in secondary cutoff with molar ratio from FA:Cs = 100:0 to 70:30. The work function (WF) was calculated by subtracting secondary cutoff energy from the energy of exciting radiation

(He I, 21.2 eV), assuming a Fermi level of 0 eV as a reference. The secondary cutoff energies were estimated as the x -axis coordinates of the intersecting points of two tangents. As the Cs molar proportion was increased from 0% to 10%, the WF slightly decreased from ~ 4.73 eV to ~ 4.66 eV (Figure S10A). Further increase in the Cs molar proportion from 10% to 20% caused a slight increase in WF from ~ 4.66 eV to ~ 4.76 eV. The WF did not change with further increase in Cs molar proportion to 30%. The VBM was determined by calculating the energy offset between the WF and IE; the energy offset was almost the same (~ 0.98 eV) at all FA:Cs ratios (Figure S10B). The VBM did not change much with FA:Cs molar proportion because the VBM of MHPs is determined mainly by the Pb s orbital and the halogen p orbital.⁶⁵ IE was lowest at FA:Cs = 90:10 (Table S5).

XPS analysis of $\text{FA}_{1-x}\text{Cs}_x\text{PbBr}_3$ polycrystalline films provides information about chemical species and bonding states at the film surface (Figures S11, S12, S13). The survey spectra showed the distinct peaks of Cs 3d, N 1s, C 1s, Pb 4f, and Br 3d orbitals (Figure S11). To identify the bonding status of each species, the Cs 3d, N 1s, Pb 4f, and Br 3d spectra were each deconvoluted by fitting Gaussian–Lorentzian curves (Figure S12). All peak positions were considered using the Au $4f_{7/2}$ peak at 84.0 eV as a reference. In the Cs 3d and N 1s spectra, the gradual increase in the Cs molar proportion of $\text{FA}_{1-x}\text{Cs}_x\text{PbBr}_3$ polycrystalline films was verified by the gradually increasing height of Cs 3d peaks (at 723.90–724.25 eV for Cs $3d_{5/2}$; at 737.85–738.15 eV for Cs $3d_{3/2}$) (Figure

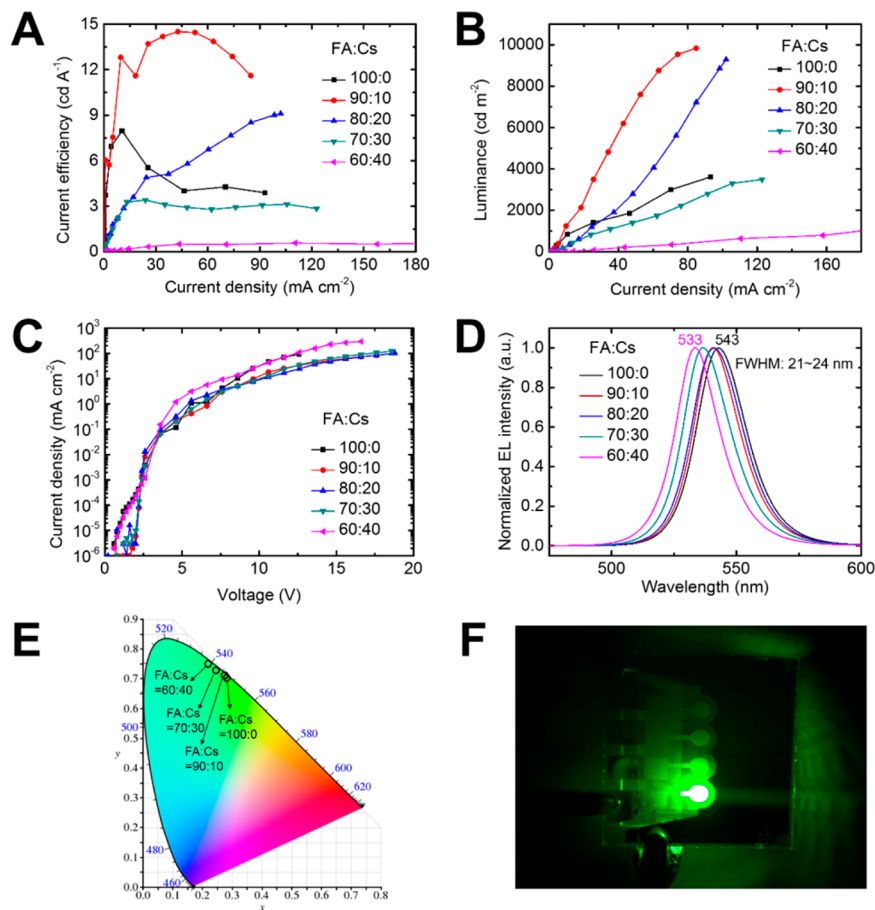


Figure 4. (A) CE, (B) luminance, (C) current density, and (D) EL spectra of $\text{FA}_{1-x}\text{Cs}_x\text{PbBr}_3$ PeLEDs with various FA:Cs molar ratios. (E) CIE coordinates at different FA:Cs molar ratios. (F) Photograph of an operating $\text{FA}_{0.9}\text{Cs}_{0.1}\text{PbBr}_3$ PeLED.

S13A) and the gradually decreasing height of the N 1s peak at 399.65–399.95 eV (Figure S13B) because the N 1s peak can be assigned to (N*–C–N)⁺ bonds of FA⁺ cations. Gradual peak shifts of up to ~0.4 eV toward lower binding energy were observed for all elements with increasing Cs molar proportion from 0 to 30 mol % (Figure S13). We attribute these peak shifts to the lower electronegativity of Cs⁺ cations than FA⁺ cations. Cs⁺ pulls electrons of adjacent nuclei less strongly than FA⁺ does. Therefore, Cs⁺ leaves less positive effective charge at the other nuclei than FA⁺ does and correspondingly decreases the binding energy in XPS. The Br 3d spectra showed the peaks at 67.43–67.81 eV (Br 3d_{5/2}) and 68.46–68.83 eV (Br 3d_{3/2}) (Figure S12D, Figure S13D), which matches well with a previous report.² Metallic Pb peaks were not observed in Pb 4f spectra (Figures S12C, S13C).

We fabricated FA_{1-x}Cs_xPbBr₃ PeLEDs and measured their current–voltage–luminance characteristics. The polycrystalline pure FAPbBr₃ PeLED had CE_{max} = 7.96 cd A⁻¹, which is slightly lower than that of a PeLED based on FAPbBr₃ nanoparticles (9.16 cd A⁻¹).¹⁶ Incorporation of 10 mol % Cs⁺ cations increased CE_{max} from 7.96 cd A⁻¹ to 14.5 cd A⁻¹ and also increased maximum luminance (*L*_{max}) from 3617 cd m⁻² to 9834 cd m⁻² (Figure 4A,B, Table 1). CE_{max} = 14.5 cd

Table 1. CE_{max}, EQE_{max}, *L*_{max}, EL Peak Position, and CIE Coordinates of FA_{1-x}Cs_xPbBr₃ PeLEDs with Varying FA:Cs Molar Ratios

FA:Cs (mol:mol)	CE _{max} (cd A ⁻¹)	EQE _{max} (%)	<i>L</i> _{max} (cd m ⁻²)	EL peak position (nm)	CIE coordinates (x, y)
100:0	7.96	1.69	3617	543	0.2828, 0.7024
90:10	14.5	3.10	9834	541	0.2746, 0.7098
80:20	9.10	1.96	9288	541	0.2711, 0.7118
70:30	2.85	0.739	3492	537	0.2451, 0.7313
60:40	1.26	0.282	3712	533	0.2177, 0.7496

A⁻¹ corresponds to a EQE_{max} = 3.10% (Table 1). To the best of our knowledge, this is the highest CE among the reported PeLEDs based on FA-Cs mixed cations. As the Cs molar proportion was further increased from 10 mol % to 40 mol %, CE and *L* gradually decreased (Figure 4A,B, Table 1). The increase in CE by the 10 mol % incorporation of Cs can be attributed to the increased PLQE of FA_{0.9}Cs_{0.1}PbBr₃ emission layers that results from the reduction in MHP grain size and trap density, as discussed above. The decrease in CE with further increase in Cs molar proportion from 10% is a result of (1) the decreased crystallinity and purity, (2) increased trap density, and (3) consequently decreased PLQE. The turn-on voltage was ~3.6 V for all PeLEDs. The EL spectra of FA_{1-x}Cs_xPbBr₃ PeLEDs showed a very narrow spectral width (fwhm = 21–24 nm), which is much smaller than those of organic LEDs (~40 nm) and QD LEDs (~30 nm, based on conventional inorganic QDs such as ZnS/CdSe) (Figure 4D).² The peak in EL spectra gradually shifted from 543 nm (FAPbBr₃) to 533 nm (FA_{0.6}Cs_{0.4}PbBr₃) (Figure 4D); this trend is consistent with the gradual changes in crystal structures (Figure 1E, Figures S3, S4) and optical band gap (Figure 2A, Figure S5). Also, this EL peak shift indicates that the emission color can be tuned from emerald green (at ~540 nm) to pure green (at ~520 nm) as represented by Commission Internationale de l'Éclairage (CIE) coordinates, by controlling the FA:Cs molar ratio (Figure 4E, Table 1); this ability can be beneficial for display applications. All pixels of FA_{1-x}Cs_xPbBr₃

PeLEDs emitted green light uniformly (Figure 4F). The operational lifetime of the FA_{0.9}Cs_{0.1}PbBr₃ PeLED was measured in comparison with a MAPbBr₃ PeLED at the same device structure (SOCP/MHP/TPBI/LiF/Al) (Figure S14). The FA_{0.9}Cs_{0.1}PbBr₃ PeLED exhibited slower luminance decay (~38 min to 50% of initial luminance of ~100 cd m⁻²) and a smaller shift in operating voltage (0.092 V min⁻¹) than did the MAPbBr₃ PeLED (~10 min to 50% of initial luminance of ~100 cd m⁻² and 0.178 V min⁻¹). The main degradation mechanism in the PeLED is probably different from the mechanism of the photoinduced PL decrease because the electric field is involved in the degradation of the PeLED. These short operational lifetimes of both the PeLEDs may be mainly caused by electric-field-driven migration of constituent ions of MHPs, subsequent accumulation of the migrated ions at interfaces, and consequent degradation of MHP layers at the interfaces.^{66–68} The slightly longer operational lifetime of FA_{0.9}Cs_{0.1}PbBr₃ PeLED than that of MAPbBr₃ PeLED may be attributed to fewer trap states in the FA_{0.9}Cs_{0.1}PbBr₃ layer³⁵ and a smaller amount of electrochemical degradation by trapped charges.⁶⁶ The elucidation of the degradation mechanism of PeLED requires further systematic characterizations of PeLED (such as transient EL, capacitance voltage, impedance) at different degradation stages.⁶⁹

CONCLUSIONS

We have realized high-efficiency polycrystalline FA_{1-x}Cs_xPbBr₃ PeLEDs with a CE_{max} of 14.5 cd A⁻¹, which is the highest reported efficiency among PeLEDs based on FA-Cs mixed MHPs. The high efficiency was achieved by fabricating uniform full-coverage FA_{1-x}Cs_xPbBr₃ polycrystalline films simply from precursor solutions and optimizing the FA:Cs molar proportion; the process does not use QDs. As the Cs molar proportion increased, the lattice constant and crystallinity gradually decreased and the PL spectrum gradually blue-shifted. The gradual changes in peak positions of XRD patterns, XPS, and steady-state PL and EL spectra demonstrated that the FA_{1-x}Cs_xPbBr₃ polycrystalline films were composed of a single phase. At the optimum composition (FA:Cs = 90:10 (mol:mol)), the average grain size decreased from 325 nm to 199 nm and the IE had the minimum value of ~5.64 eV. PLQE, PL lifetime, and temperature-dependent PL measurement showed that the inclusion of a small proportion (~10 mol %) of Cs⁺ cations in FAPbBr₃ increases PLQE and PL lifetime and suppresses the thermally induced PL quenching, possibly by reducing grain size and consequently strengthening spatial confinement of charge carriers or excitons and by reducing the density of trap states. Further increase in the Cs molar proportion from 10% decreased the PLQE of the films and CE and *L* of PeLEDs, possibly as a result of the decrease in crystallinity and concomitant increase in trap density. Also, the incorporation of Cs⁺ cations increased the photostability of FA_{1-x}Cs_xPbBr₃ polycrystalline films. The decreased PL intensity was slowly recovered in the dark; this slow recovery and the absence of changes in absorbance, PL peak position, and XRD peak position after the PL decrease imply that the PL decrease in the FA_{1-x}Cs_xPbBr₃ films was not a result of decomposition of FA_{1-x}Cs_xPbBr₃, but of formation of light-induced metastable states that cause nonradiative recombination.

Our study has suggested that the fabrication of uniform polycrystalline MHP films with the optimum FA:Cs molar ratio can be a simple and effective strategy to increase EL efficiency

and brightness of FA-Cs-based green PeLEDs. However, the FA_{1-x}Cs_xPbBr₃ PeLED still has lower EL efficiency (14.5 cd A⁻¹) than the state-of-the-art MAPbBr₃ PeLEDs (42.9 cd A⁻¹).² Therefore, further studies should be conducted to identify EL efficiency limitations and to develop strategies to overcome them. The introduction of a Ruddlesden–Popper phase to FA-Cs-based MHPs may be an effective solution to suppress exciton dissociation with increased effective exciton binding energy and increase geminate recombination. Also, the incorporation of a small proportion of additives to FA-Cs-based MHPs may lead to *in situ* formation of nanocrystals in the bulk polycrystalline films and thereby increase EL efficiency.²⁰ Furthermore, passivation methods that reduce the trap density of MHP films may be effective to increase radiative recombination; for example, the surface passivation by using trioctylphosphine oxide⁷⁰ or amine derivatives⁷¹ can increase luminescence efficiency. Ultimately, the chemical structure of passivation agents that can heal the defects of MHP polycrystalline films most effectively must be identified, and effective processes to include the passivation agents in MHP emission layers without blocking charge transport must be developed. We envision that these approaches to fabrication of high-efficiency PeLEDs may become a core next-generation technology in the display and lighting industries and in academic societies that study light emitters and optoelectronics.

METHODS AND EXPERIMENTAL DETAILS

Fabrication of MHP Polycrystalline Films. FA_{1-x}Cs_xPbBr₃ solutions (30.0 wt %) were prepared by mixing FABr (Dyesol), CsBr (Aldrich), and PbBr₂ (Aldrich) in DMSO in appropriate FA:Cs molar ratio, with (FABr + CsBr):PbBr₂ molar ratio = 1.1:1. Low-conductivity SOCP layers (40 nm) were formed on cleaned glass or Si native wafer substrates as previously reported.² Then FA_{1-x}Cs_xPbBr₃ solutions were spin-coated onto the SOCP layers in a N₂ atmosphere (stage 1:500 rpm for 7 s, stage 2:3000 rpm for 90 s). During stage 2, an additive-based nanocrystal-pinning process that induces immediate crystallization of MHPs by washing out DMSO with a chloroform/TPBI solution² was applied to the spinning substrates after 30 s. Then the FA_{1-x}Cs_xPbBr₃ films were baked on a hot plate at 70 °C for 10 min.

LED Fabrication and Characterization. Glass/SOCP/FA_{1-x}Cs_xPbBr₃ was fabricated as mentioned above, except that 100-nm-thick high-conductivity SOCP anodes² were formed instead of the low-conductivity SOCP layers. On the FA_{1-x}Cs_xPbBr₃ layers, TPBI (50 nm), LiF (1 nm), and Al (100 nm) were thermally deposited in sequence in a high-vacuum chamber. Then each device was encapsulated in a N₂ atmosphere.

SEM Measurement. SEM images of Si wafer/SOCP/FA_{1-x}Cs_xPbBr₃ films were measured using a field emission SEM (MERLIN compact, ZEISS) at the Research Institute of Advanced Materials, Seoul National University.

Steady-State PL Measurement. Steady-state PL of glass/SOCP/FA_{1-x}Cs_xPbBr₃ or quartz/FA_{1-x}Cs_xPbBr₃ samples was measured using a spectrofluorometer (JASCO FP6500) without sample encapsulation. A continuous-output xenon arc lamp with a power of 150 W was used as an excitation source, and the excitation wavelength was 405 nm. For the photostability measurement, quartz substrates were used instead of glass/SOCP. The light was incident on the quartz side that is opposite the FA_{1-x}Cs_xPbBr₃/air interface.

PLQE Measurement. PLQE of quartz/FA_{1-x}Cs_xPbBr₃ samples was measured using the same integrating sphere method reported previously (a continuous-wave 405 nm laser diode with a power density of 900 mW cm⁻²).^{2,72}

TCSPC Measurement. TCSPC measurement of quartz/FA_{1-x}Cs_xPbBr₃/PMMA samples was conducted using the same equipment and procedure described elsewhere,² except a different TCSPC module was used (PicoHarp 260, PicoQuant). Instrument

response function (IRF) was ignored because the PL lifetime curves were much longer than the temporal width of the IRF. The excitation power density was ~25 mW cm⁻².

XPS and UPS Measurement. XPS and UPS spectra of ITO/SOCP/FA_{1-x}Cs_xPbBr₃ films were measured using the same procedures reported previously² in collaboration with Korea Basic Science Institute (KBSI).

ASSOCIATED CONTENT

Supporting Information

The Supporting Information is available free of charge on the ACS Publications website at DOI: 10.1021/acsnano.8b00409.

Additional SEM images and grain size calculation; additional analysis of XRD, steady-state PL, absorption, TCSPC, temperature-dependent PL, photostability results; UPS and XPS analysis; device operational lifetime (PDF)

AUTHOR INFORMATION

Corresponding Author

*E-mail: twlees@snu.ac.kr, taewlees@gmail.com.

ORCID

Aditya Sadhanala: 0000-0003-2832-4894

Vijay Venugopalan: 0000-0003-4701-5536

Richard H. Friend: 0000-0001-6565-6308

Tae-Woo Lee: 0000-0002-6449-6725

Author Contributions

*H. Cho and J. S. Kim contributed equally to this work.

Notes

The authors declare no competing financial interest.

ACKNOWLEDGMENTS

This work was supported by the National Research Foundation of Korea (NRF) grant funded by the Korea government (MSIT) (NRF-2016R1A3B1908431). The authors thank C.-K. Moon and J.-S. Huh for helping to investigate the PLQE trend.

REFERENCES

- (1) Kim, Y.-H.; Cho, H.; Lee, T.-W. Metal Halide Perovskite Light Emitters. *Proc. Natl. Acad. Sci. U. S. A.* **2016**, *113*, 11694–11702.
- (2) Cho, H.; Jeong, S.-H.; Park, M.-H.; Kim, Y.-H.; Wolf, C.; Lee, C.-L.; Heo, J. H.; Sadhanala, A.; Myoung, N.; Yoo, S.; Im, S. H.; Friend, R. H.; Lee, T.-W. Overcoming the Electroluminescence Efficiency Limitations of Perovskite Light-Emitting Diodes. *Science* **2015**, *350*, 1222–1225.
- (3) Tan, Z.-K.; Moghaddam, R. S.; Lai, M. L.; Docampo, P.; Higler, R.; Deschler, F.; Price, M.; Sadhanala, A.; Pazos, L. M.; Credgington, D.; Hanusch, F.; Bein, T.; Snaith, H. J.; Friend, R. H. Bright Light-Emitting Diodes Based on Organometal Halide Perovskite. *Nat. Nanotechnol.* **2014**, *9*, 687–692.
- (4) Kim, Y.-H.; Cho, H.; Heo, J. H.; Kim, T.-S.; Myoung, N.; Lee, C.-L.; Im, S. H.; Lee, T.-W. Multicolored Organic/Inorganic Hybrid Perovskite Light-Emitting Diodes. *Adv. Mater.* **2015**, *27*, 1248–1254.
- (5) Yu, J. C.; Kim, D. B.; Baek, G.; Lee, B. R.; Jung, E. D.; Lee, S.; Chu, J. H.; Lee, D. K.; Choi, K. J.; Cho, S.; Song, M. H. High-Performance Planar Perovskite Optoelectronic Devices: A Morphological and Interfacial Control by Polar Solvent Treatment. *Adv. Mater.* **2015**, *27*, 3492–3500.
- (6) Xing, G.; Mathews, N.; Lim, S. S.; Yantara, N.; Liu, X.; Sabba, D.; Grätzel, M.; Mhaisalkar, S.; Sum, T. C. Low-Temperature Solution-Processed Wavelength-Tunable Perovskites for Lasing. *Nat. Mater.* **2014**, *13*, 476–480.

- (7) Xu, W.; Cho, H.; Kim, Y. H.; Kim, Y. T.; Wolf, C.; Park, C. G.; Lee, T. W. Organometal Halide Perovskite Artificial Synapses. *Adv. Mater.* **2016**, *28*, 5916–5922.
- (8) Yang, W. S.; Noh, J. H.; Jeon, N. J.; Kim, Y. C.; Ryu, S.; Seo, J.; Seok, S. I. High-Performance Photovoltaic Perovskite Layers Fabricated through Intramolecular Exchange. *Science* **2015**, *348*, 1234–1237.
- (9) Miyata, A.; Mitioglu, A.; Plochocka, P.; Portugall, O.; Wang, J. T.; Stranks, S. D.; Snaith, H. J.; Nicholas, R. J. Direct Measurement of the Exciton Binding Energy and Effective Masses for Charge Carriers in Organic-Inorganic Tri-Halide Perovskites. *Nat. Phys.* **2015**, *11*, 582–587.
- (10) Yuan, Y.; Huang, J. Ion Migration in Organometal Trihalide Perovskite and Its Impact on Photovoltaic Efficiency and Stability. *Acc. Chem. Res.* **2016**, *49*, 286–293.
- (11) Seo, H.-K.; Kim, H.; Lee, J.; Park, M.-H.; Jeong, S.-H.; Kim, Y.-H.; Kwon, S.-J.; Han, T.-H.; Yoo, S.; Lee, T.-W. Efficient Flexible Organic/Inorganic Hybrid Perovskite Light-Emitting Diodes Based on Graphene Anode. *Adv. Mater.* **2017**, *29*, 1605587.
- (12) Byun, J.; Cho, H.; Wolf, C.; Jang, M.; Sadhanala, A.; Friend, R. H.; Yang, H.; Lee, T.-W. Efficient Visible Quasi-2D Perovskite Light-Emitting Diodes. *Adv. Mater.* **2016**, *28*, 7515–7520.
- (13) Yuan, M.; Quan, L. N.; Comin, R.; Walters, G.; Sabatini, R.; Voznyy, O.; Hoogland, S.; Zhao, Y.; Beauregard, E. M.; Kanjanaboos, P.; Lu, Z.; Kim, D. H.; Sargent, E. H. Perovskite Energy Funnels for Efficient Light-Emitting Diodes. *Nat. Nanotechnol.* **2016**, *11*, 872–879.
- (14) Wang, N.; Cheng, L.; Ge, R.; Zhang, S.; Miao, Y.; Zou, W.; Yi, C.; Sun, Y.; Cao, Y.; Yang, R.; Wei, Y.; Guo, Q.; Ke, Y.; Yu, M.; Jin, Y.; Liu, Y.; Ding, Q.; Di, D.; Yang, L.; et al. Perovskite Light-Emitting Diodes Based on Solution-Processed Self-Organized Multiple Quantum Wells. *Nat. Nat. Photonics* **2016**, *10*, 699–704.
- (15) Xiao, Z.; Kerner, R. A.; Zhao, L.; Tran, N. L.; Lee, K. M.; Koh, T.-W.; Scholes, G. D.; Rand, B. P. Efficient Perovskite Light-Emitting Diodes Featuring Nanometre-Sized Crystallites. *Nat. Nat. Photonics* **2017**, *11*, 108–115.
- (16) Kim, Y.-H.; Lee, G.-H.; Kim, Y.-T.; Wolf, C.; Yun, H. J.; Kwon, W.; Park, C. G.; Lee, T.-W. High Efficiency Perovskite Light-Emitting Diodes of Ligand-Engineered Colloidal Formamidinium Lead Bromide Nanoparticles. *Nano Energy* **2017**, *38*, 51–58.
- (17) Jeong, S.-H.; Woo, S.-H.; Han, T.-H.; Park, M.-H.; Cho, H.; Kim, Y.-H.; Cho, H.; Kim, H.; Yoo, S.; Lee, T.-W. Universal High Work Function Flexible Anode for Simplified ITO-Free Organic and Perovskite Light-Emitting Diodes with Ultra-High Efficiency. *NPG Asia Mater.* **2017**, *9*, e411.
- (18) Kim, Y.-H.; Wolf, C.; Kim, Y.-T.; Cho, H.; Kwon, W.; Do, S.; Sadhanala, A.; Park, C. G.; Rhee, S.-W.; Im, S. H.; Friend, R. H.; Lee, T.-W. Highly Efficient Light-Emitting Diodes of Colloidal Metal-Halide Perovskite Nanocrystals beyond Quantum Size. *ACS Nano* **2017**, *11*, 6586–6593.
- (19) Quan, L. N.; Zhao, Y.; García De Arquer, F. P.; Sabatini, R.; Walters, G.; Voznyy, O.; Comin, R.; Li, Y.; Fan, J. Z.; Tan, H.; Pan, J.; Yuan, M.; Bakr, O. M.; Lu, Z.; Kim, D. H.; Sargent, E. H. Tailoring the Energy Landscape in Quasi-2D Halide Perovskites Enables Efficient Green-Light Emission. *Nano Lett.* **2017**, *17*, 3701–3709.
- (20) Zhao, L.; Yeh, Y.-W.; Tran, N. L.; Wu, F.; Xiao, Z.; Kerner, R. A.; Lin, Y. L.; Scholes, G. D.; Yao, N.; Rand, B. P. In Situ Preparation of Metal Halide Perovskite Nanocrystal Thin Films for Improved Light-Emitting Devices. *ACS Nano* **2017**, *11*, 3957–3964.
- (21) Congreve, D. N.; Weidman, M. C.; Seitz, M.; Paritmongkol, W.; Dahod, N. S.; Tisdale, W. A. Tunable Light-Emitting Diodes Utilizing Quantum-Confined Layered Perovskite Emitters. *ACS Photonics* **2017**, *4*, 476–481.
- (22) Zhang, X.; Liu, H.; Wang, W.; Zhang, J.; Xu, B.; Karen, K. L.; Zheng, Y.; Liu, S.; Chen, S.; Wang, K.; Sun, X. W. Hybrid Perovskite Light-Emitting Diodes Based on Perovskite Nanocrystals with Organic-Inorganic Mixed Cations. *Adv. Mater.* **2017**, *29*, 1606405.
- (23) Perumal, A.; Shendre, S.; Li, M.; Tay, Y. K. E.; Sharma, V. K.; Chen, S.; Wei, Z.; Liu, Q.; Gao, Y.; Buenconsejo, P. J. S.; Tan, S. T.; Gan, C. L.; Xiong, Q.; Sum, T. C.; Demir, H. V. High Brightness Formamidinium Lead Bromide Perovskite Nanocrystal Light Emitting Devices. *Sci. Rep.* **2016**, *6*, 36733.
- (24) Pan, J.; Quan, L. N.; Zhao, Y.; Peng, W.; Murali, B.; Sarmah, S. P.; Yuan, M.; Sinatra, L.; Alyami, N. M.; Liu, J.; Yassitepe, E.; Yang, Z.; Voznyy, O.; Comin, R.; Hedhili, M. N.; Mohammed, O. F.; Lu, Z. H.; Kim, D. H.; Sargent, E. H.; et al. Highly Efficient Perovskite-Quantum-Dot Light-Emitting Diodes by Surface Engineering. *Adv. Mater.* **2016**, *28*, 8718–8725.
- (25) Kumar, S.; Jagielski, J.; Kallikounis, N.; Kim, Y.-H.; Wolf, C.; Jenny, F.; Tian, T.; Hofer, C. J.; Chiu, Y.-C.; Stark, W. J.; Lee, T.-W.; Shih, C.-J. Ultrapure Green Light-Emitting Diodes Using Two-Dimensional Formamidinium Perovskites: Achieving Recommendation 2020 Color Coordinates. *Nano Lett.* **2017**, *17*, S277–S284.
- (26) Yang, S.; Wang, Y.; Liu, P.; Cheng, Y.-B.; Zhao, H. J.; Yang, H. G. Functionalization of Perovskite Thin Films with Moisture-Tolerant Molecules. *Nat. Energy* **2016**, *1*, 15016.
- (27) Saliba, M.; Matsui, T.; Domanski, K.; Seo, J.-Y.; Ummadisingu, A.; Zakeeruddin, S. M.; Correa-Baena, J.-P.; Tress, W. R.; Abate, A.; Hagfeldt, A.; Grätzel, M. Incorporation of Rubidium Cations into Perovskite Solar Cells Improves Photovoltaic Performance. *Science* **2016**, *354*, 206–209.
- (28) Yoon, S. J.; Stampelcoskie, K. G.; Kamat, P. V. How Lead Halide Complex Chemistry Dictates the Composition of Mixed Halide Perovskites. *J. Phys. Chem. Lett.* **2016**, *7*, 1368–1373.
- (29) McMeekin, D. P.; Sadoughi, G.; Rehman, W.; Eperon, G. E.; Saliba, M.; Horantner, M. T.; Haghighirad, A.; Sakai, N.; Korte, L.; Rech, B.; Johnston, M. B.; Herz, L. M.; Snaith, H. J. A Mixed-Cation Lead Mixed-Halide Perovskite Absorber for Tandem Solar Cells. *Science* **2016**, *351*, 151–155.
- (30) Niu, G.; Li, W.; Meng, F.; Wang, L.; Dong, H.; Qiu, Y. Study on the Stability of $\text{CH}_3\text{NH}_3\text{PbI}_3$ Films and the Effect of Post-Modification by Aluminum Oxide in All-Solid-State Hybrid Solar Cells. *J. Mater. Chem. A* **2014**, *2*, 705–710.
- (31) Zhao, X.; Park, N.-G. Stability Issues on Perovskite Solar Cells. *Photonics* **2015**, *2*, 1139–1151.
- (32) Kim, Y.-H.; Cho, H.; Heo, J. H.; Im, S. H.; Lee, T.-W. Effects of Thermal Treatment on Organic-Inorganic Hybrid Perovskite Films and Luminous Efficiency of Light-Emitting Diodes. *Curr. Appl. Phys.* **2016**, *16*, 1069–1074.
- (33) Hanusch, F. C.; Wiesenmayer, E.; Mankel, E.; Binek, A.; Angloher, P.; Fraunhofer, C.; Giesbrecht, N.; Feckl, J. M.; Jaegermann, W.; Johrendt, D.; Bein, T.; Docampo, P. Efficient Planar Heterojunction Perovskite Solar Cells Based on Formamidinium Lead Bromide. *J. Phys. Chem. Lett.* **2014**, *5*, 2791–2795.
- (34) Zhumekenov, A. A.; Saidaminov, M. I.; Haque, M. A.; Alarousu, E.; Sarmah, S. P.; Murali, B.; Dursun, I.; Miao, X.-H.; Abdelhady, A. L.; Wu, T.; Mohammed, O. F.; Bakr, O. M. Formamidinium Lead Halide Perovskite Crystals with Unprecedented Long Carrier Dynamics and Diffusion Length. *ACS Energy Lett.* **2016**, *1*, 32–37.
- (35) Lee, J.-W.; Kim, D.-H.; Kim, H.-S.; Seo, S.-W.; Cho, S. M.; Park, N.-G. Formamidinium and Cesium Hybridization for Photo- and Moisture-Stable Perovskite Solar Cell. *Adv. Energy Mater.* **2015**, *5*, 1501310.
- (36) Rehman, W.; McMeekin, D. P.; Patel, J. B.; Milot, R. L.; Johnston, M. B.; Snaith, H. J.; Herz, L. M. Photovoltaic Mixed-Cation Lead Mixed-Halide Perovskites: Links between Crystallinity, Photo-Stability and Electronic Properties. *Energy Environ. Sci.* **2017**, *10*, 361–369.
- (37) Saidaminov, M. I.; Abdelhady, A. L.; Murali, B.; Alarousu, E.; Burlakov, V. M.; Peng, W.; Dursun, I.; Wang, L.; He, Y.; Maculan, G.; Goriely, A.; Wu, T.; Mohammed, O. F.; Bakr, O. M. High-Quality Bulk Hybrid Perovskite Single Crystals within Minutes by Inverse Temperature Crystallization. *Nat. Commun.* **2015**, *6*, 7586.
- (38) Meng, L.; Yao, E.-P.; Hong, Z.; Chen, H.; Sun, P.; Yang, Z.; Li, G.; Yang, Y. Pure Formamidinium-Based Perovskite Light-Emitting Diodes with High Efficiency and Low Driving Voltage. *Adv. Mater.* **2017**, *29*, 1603826.
- (39) Protesescu, L.; Yakunin, S.; Bodnarchuk, M. I.; Krieg, F.; Caputo, R.; Hendon, C. H.; Yang, R. X.; Walsh, A.; Kovalenko, M. V.

Nanocrystals of Cesium Lead Halide Perovskites (CsPbX_3 , $\text{X} = \text{Cl}$, Br , and I): Novel Optoelectronic Materials Showing Bright Emission with Wide Color Gamut. *Nano Lett.* **2015**, *15*, 3692–3696.

(40) Kulbak, M.; Gupta, S.; Kedem, N.; Levine, I.; Bendikov, T.; Hodes, G.; Cahen, D. Cesium Enhances Long-Term Stability of Lead Bromide Perovskite-Based Solar Cells. *J. Phys. Chem. Lett.* **2016**, *7*, 167–172.

(41) Swarnkar, A.; Chuliyil, R.; Ravi, V. K.; Irfanullah, M.; Chowdhury, A.; Nag, A. Colloidal CsPbBr_3 Perovskite Nanocrystals: Luminescence beyond Traditional Quantum Dots. *Angew. Chem., Int. Ed.* **2015**, *54*, 15424–15428.

(42) Yantara, N.; Bhaumik, S.; Yan, F.; Sabba, D.; Dewi, H. A.; Mathews, N.; Boix, P. P.; Demir, H. V.; Mhaisalkar, S. Inorganic Halide Perovskites for Efficient Light-Emitting Diodes. *J. Phys. Chem. Lett.* **2015**, *6*, 4360–4364.

(43) Van Le, Q.; Park, M.; Sohn, W.; Jang, H. W.; Kim, S. Y. Investigation of Energy Levels and Crystal Structures of Cesium Lead Halides and Their Application in Full-Color Light-Emitting Diodes. *Adv. Electron. Mater.* **2017**, *3*, 1600448.

(44) Stoumpos, C. C.; Malliakas, C. D.; Peters, J. A.; Liu, Z.; Sebastian, M.; Im, J.; Chasapis, T. C.; Wibowo, A. C.; Chung, D. Y.; Freeman, A. J.; Wessels, B. W.; Kanatzidis, M. G. Crystal Growth of the Perovskite Semiconductor CsPbBr_3 : A New Material for High-Energy Radiation Detection. *Cryst. Growth Des.* **2013**, *13*, 2722–2727.

(45) Wei, Z.; Perumal, A.; Su, R.; Sushant, S.; Xing, J.; Zhang, Q.; Tan, S. T.; Demir, H. V.; Xiong, Q. Solution-Processed Highly Bright and Durable Cesium Lead Halide Perovskite Light-Emitting Diodes. *Nanoscale* **2016**, *8*, 18021–18026.

(46) Cho, H.; Wolf, C.; Kim, J. S.; Yun, H. J.; Bae, J. S.; Kim, H.; Heo, J.-M.; Ahn, S.; Lee, T.-W. High-Efficiency Solution-Processed Inorganic Metal Halide Perovskite Light-Emitting Diodes. *Adv. Mater.* **2017**, *29*, 1700579.

(47) Yi, C.; Luo, J.; Meloni, S.; Boziki, A.; Ashari-Astani, N.; Grätzel, C.; Zakeeruddin, S. M.; R  thlisberger, U.; Grätzel, M. Entropic Stabilization of Mixed A-Cation ABX_3 Metal Halide Perovskites for High Performance Perovskite Solar Cells. *Energy Environ. Sci.* **2016**, *9*, 656–662.

(48) Li, Z.; Yang, M.; Park, J.-S.; Wei, S.-H.; Berry, J. J.; Zhu, K. Stabilizing Perovskite Structures by Tuning Tolerance Factor: Formation of Formamidinium and Cesium Lead Iodide Solid-State Alloys. *Chem. Mater.* **2016**, *28*, 284–292.

(49) Amat, A.; Mosconi, E.; Ronca, E.; Quarti, C.; Umari, P.; Nazeeruddin, M. K.; Grätzel, M.; De Angelis, F. Cation-Induced Band-Gap Tuning in Organohalide Perovskites: Interplay of Spin-Orbit Coupling and Octahedra Tilting. *Nano Lett.* **2014**, *14*, 3608–3616.

(50) Weber, O. J.; Charles, B.; Weller, M. T. Phase Behaviour and Composition in the Formamidinium–methylammonium Hybrid Lead Iodide Perovskite Solid Solution. *J. Mater. Chem. A* **2016**, *4*, 15375–15382.

(51) Wu, C.-G.; Chiang, C.-H.; Chang, S. H. A Perovskite Cell with a Record-High-Voc of 1.61 V Based on Solvent Annealed $\text{CH}_3\text{NH}_3\text{PbBr}_3/\text{ICBA}$ Active Layer. *Nanoscale* **2016**, *8*, 4077–4085.

(52) Prasanna, R.; Gold-Parker, A.; Leijtens, T.; Conings, B.; Babayigit, A.; Boyen, H.-G.; Toney, M. F.; McGehee, M. D. Band Gap Tuning via Lattice Contraction and Octahedral Tilting in Perovskite Materials for Photovoltaics. *J. Am. Chem. Soc.* **2017**, *139*, 11117–11124.

(53) Knutson, J. R.; Beechem, J. M.; Brand, L. Simultaneous Analysis of Multiple Fluorescence Decay Curves: A Global Approach. *Chem. Phys. Lett.* **1983**, *102*, 501–507.

(54) Li, J.; Yuan, X.; Jing, P.; Li, J.; Wei, M.; Hua, J.; Zhao, J.; Tian, L. Temperature-Dependent Photoluminescence of Inorganic Perovskite Nanocrystal Films. *RSC Adv.* **2016**, *6*, 78311–78316.

(55) Yang, M.; Zeng, Y.; Li, Z.; Kim, D. H.; Jiang, C.-S.; van de Lagemaat, J.; Zhu, K. Do Grain Boundaries Dominate Non-Radiative Recombination in $\text{CH}_3\text{NH}_3\text{PbI}_3$ Perovskite Thin Films? *Phys. Chem. Chem. Phys.* **2017**, *19*, 5043–5050.

(56) Wang, B.; Wong, K. Y.; Yang, S.; Chen, T. Crystallinity and Defect State Engineering in Organo-Lead Halide Perovskite for High-Efficiency Solar Cells. *J. Mater. Chem. A* **2016**, *4*, 3806–3812.

(57) de Quilletes, D. W.; Vorpahl, S. M.; Stranks, S. D.; Nagaoka, H.; Eperon, G. E.; Ziffer, M. E.; Snaith, H. J.; Ginger, D. S. Impact of Microstructure on Local Carrier Lifetime in Perovskite Solar Cells. *Science* **2015**, *348*, 683–686.

(58) Baumann, A.; V  th, S.; Rieder, P.; Heiber, M. C.; Tvingstedt, K.; Dyakonov, V. Identification of Trap States in Perovskite Solar Cells. *J. Phys. Chem. Lett.* **2015**, *6*, 2350–2354.

(59) Gottesman, R.; Gouda, L.; Kalanoor, B. S.; Haltzi, E.; Tirosh, S.; Rosh-Hodesh, E.; Tischler, Y.; Zaban, A.; Quarti, C.; Mosconi, E.; De Angelis, F. Photoinduced Reversible Structural Transformations in Free-Standing $\text{CH}_3\text{NH}_3\text{PbI}_3$ Perovskite Films. *J. Phys. Chem. Lett.* **2015**, *6*, 2332–2338.

(60) Nie, W.; Blancon, J.-C.; Neukirch, A. J.; Appavoo, K.; Tsai, H.; Chhowalla, M.; Alam, M. A.; Sfeir, M. Y.; Katan, C.; Even, J.; Tretiak, S.; Crochet, J. J.; Gupta, G.; Mohite, A. D. Light-Activated Photocurrent Degradation and Self-Healing in Perovskite Solar Cells. *Nat. Commun.* **2016**, *7*, 11574.

(61) Hentz, O.; Zhao, Z.; Grade  ak, S. Impacts of Ion Segregation on Local Optical Properties in Mixed Halide Perovskite Films. *Nano Lett.* **2016**, *16*, 1485–1490.

(62) Yuan, H.; Debroye, E.; Janssen, K.; Naiki, H.; Steuwe, C.; Lu, G.; Moris, M.; Orgiu, E.; Uji-i, H.; De Schryver, F.; Samor  , P.; Hofkens, J.; Roelofs, M. Degradation of Methylammonium Lead Iodide Perovskite Structures through Light and Electron Beam Driven Ion Migration. *J. Phys. Chem. Lett.* **2016**, *7*, 561–566.

(63) Huang, S.; Li, Z.; Wang, B.; Zhu, N.; Zhang, C.; Kong, L.; Zhang, Q.; Shan, A.; Li, L. Morphology Evolution and Degradation of CsPbBr_3 Nanocrystals under Blue Light-Emitting Diode Illumination. *ACS Appl. Mater. Interfaces* **2017**, *9*, 7249–7258.

(64) Tian, Y.; Peter, M.; Unger, E.; Abdellah, M.; Zheng, K.; Pullerits, T.; Yartsev, A.; Sundstr  m, V.; Scheblykin, I. G. Mechanistic Insights into Perovskite Photoluminescence Enhancement: Light Curing with Oxygen Can Boost Yield Thousandfold. *Phys. Chem. Chem. Phys.* **2015**, *17*, 24978–24987.

(65) Geng, W.; Zhang, L.; Zhang, Y.-N.; Lau, W.-M.; Liu, L.-M. First-Principles Study of Lead Iodide Perovskite Tetragonal and Orthorhombic Phases for Photovoltaics. *J. Phys. Chem. C* **2014**, *118*, 19565–19571.

(66) Ahn, N.; Kwak, K.; Jang, M. S.; Yoon, H.; Lee, B. Y.; Lee, J.; Pikhitsa, P. V.; Byun, J.; Choi, M. Trapped Charge Driven Degradation of Perovskite Solar Cells. *Nat. Commun.* **2016**, *7*, 13422.

(67) Chen, S.; Wen, X.; Sheng, R.; Huang, S.; Deng, X.; Green, M. A.; Ho-Baillie, A. Mobile Ion Induced Slow Carrier Dynamics in Organic-Inorganic Perovskite $\text{CH}_3\text{NH}_3\text{PbBr}_3$. *ACS Appl. Mater. Interfaces* **2016**, *8*, 5351–5357.

(68) Cho, H.; Kim, Y.-H.; Wolf, C.; Lee, H.-D.; Lee, T.-W. Improving the Stability of Metal Halide Perovskite Materials and Light-Emitting Diodes. *Adv. Mater.* **2018**, 1704587.

(69) Han, T.-H.; Song, W.; Lee, T.-W. Elucidating the Crucial Role of Hole Injection Layer in Degradation of Organic Light-Emitting Diodes. *ACS Appl. Mater. Interfaces* **2015**, *7*, 3117–3125.

(70) DeQuilletes, D. W.; Koch, S.; Burke, S.; Paranj, R. K.; Shropshire, A. J.; Ziffer, M. E.; Ginger, D. S. Photoluminescence Lifetimes Exceeding 8 μs and Quantum Yields Exceeding 30% in Hybrid Perovskite Thin Films by Ligand Passivation. *ACS Energy Lett.* **2016**, *1*, 438–444.

(71) Lee, S.; Park, J. H.; Lee, B. R.; Jun, E. D.; Yu, J. C.; Di Nuzzo, D.; Friend, R. H.; Song, M. H. Amine-Based Passivating Materials for Enhanced Optical Properties and Performance of Organic–Inorganic Perovskites in Light-Emitting Diodes. *J. Phys. Chem. Lett.* **2017**, *8*, 1784–1792.

(72) de Mello, J. C.; Wittmann, H. F.; Friend, R. H. An Improved Experimental Determination of External Photoluminescence Quantum Efficiency. *Adv. Mater.* **1997**, *9*, 230–232.